

Spin Excitation in Coupled Honeycomb Lattice $\text{Ni}_2\text{InSbO}_6$

Zheyuan Liu,¹ Yusuke Araki,² Taka-hisa Arima,² Shinichi Itoh,^{3,4} Shinichiro Asai,¹ and Takatsugu Masuda^{1,3,5}

¹*Institute for Solid State Physics, the University of Tokyo*

²*Department of Advanced Materials Sciences, the University of Tokyo, Kashiwa 277-8561, Japan*

³*Institute of Materials Structure Science, High Energy Accelerator Research Organization, Ibaraki 305-0801, Japan*

⁴*Materials and Life Science Division, J-PARC Center, Tokai, Ibaraki 319-1195, Japan*

⁵*Trans-scale Quantum Science Institute, The University of Tokyo, Tokyo 113-0033, Japan*

(Dated: December 13, 2022)

We performed an inelastic neutron scattering experiment on a polycrystalline sample of a helimagnet $\text{Ni}_2\text{InSbO}_6$ to construct the spin Hamiltonian. Well-defined spin-wave excitation with a band energy of 20 meV was observed below $T_N = 76$ K. Using the linear spin-wave theory, the spectrum was reasonably reproduced with honeycomb spin layers coupled along the stacking axis (the c axis). The proposed spin model reproduces the soliton lattice induced by a magnetic field applied perpendicular to the c axis.

I. INTRODUCTION

In an insulating magnet with non-centrosymmetry, Dzyaloshinskii-Moriya (DM) interaction is activated through the spin-orbit coupling [1, 2], favoring a non-collinear spin configuration, as opposed in a magnet which favors a collinear spin configuration owing to the symmetric exchange interaction. As a result of competition between the interactions, an incommensurate spin structure is often realized in the non-centrosymmetric magnet [3]. In the past decades, proper screw, conical, and cycloidal structures were experimentally observed in many compounds [4–11]. Recently intriguing magnetic textures induced by a magnetic field were reported in these helimagnets. The spin soliton lattice, where the spin arrangement follows the solution of sine-Gordon equation, was observed when a magnetic field was applied parallel to the spin rotation plane [12]. Control of the soliton lattice can be a significant technology in spintronics [13]. Néel- [14–17] and Bloch-type [18–20] skyrmions emerged in a magnetic field in polar and chiral systems, respectively. Stable magnetic skyrmions protected by non-trivial topology are promising candidates for novel magnetic memories devices [21]. DM interaction is, thus, a key term for the emergent magnetic lattices in helimagnets.

In this study, we focus on a polar-chiral $\text{Ni}_2\text{InSbO}_6$ [22] where In^{3+} and Sb^{5+} ions are substituted for Ni^{2+} and Te^{6+} ions in the parent compound Ni_3TeO_6 [23–27] which is an ordered derivative of corundum. The space group is $R\bar{3}$ with lattice parameters $a = 5.2158 \text{ \AA}$ and $c = 14.0139 \text{ \AA}$ in hexagonal notation, as shown in Fig. 1(a). The ground state of $\text{Ni}_2\text{InSbO}_6$ was reported to be a proper-screw-type structure with the propagation vector of $\mathbf{k} = 0.029\mathbf{b}^*$. The transition temperature was $T_N = 76$ K. Recent study reported two-steps transitions; the compound first turns into a commensurate layered antiferromagnetic structure, and successively changes to the proper-screw-type structure which is generated by chirality-induced DM interaction [28]. Ring-like magnetic scattering reported in several DM helimag-

nets [16, 17, 29, 30] was observed by neutron diffraction experiments, suggesting that the direction of the propagation vector is, in fact, isotropic in the ab -plane [28]. In addition, the direction was controlled by in-plane magnetic field. Combination of magnetization, electric polarization, and dielectric constant measurements revealed an enriched phase diagram including helical, soliton lattice, canted antiferromagnetic (CAF) and \mathbf{q} -flop phases [28], offering an excellent environment to study the relationship of incommensurate magnetic structures and DM interaction.

In conventional helimagnets with a fixed modulation axis, the soliton lattice is induced in the field applied in the spin rotation plane as a result of the competition between symmetric exchange and DM interaction responsible for the helical structure and Zeeman energy [12, 31–33]. In contrast in chiral polar helimagnet $\text{Ni}_2\text{InSbO}_6$, the soliton lattice was proposed to be induced when

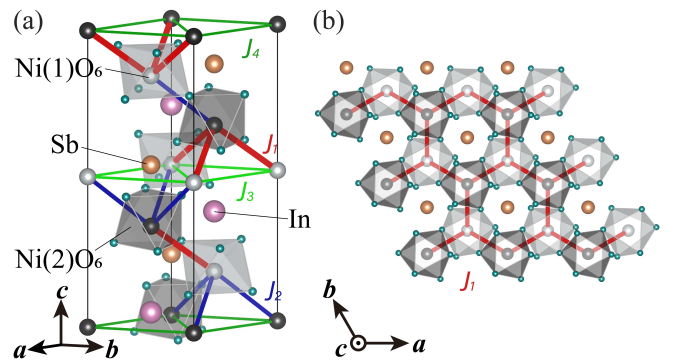


FIG. 1. (a) Crystal structure of $\text{Ni}_2\text{InSbO}_6$ and exchange paths between Ni^{2+} spins. $\text{Ni}(1)\text{O}_6$ octahedra (light gray), $\text{Ni}(2)\text{O}_6$ octahedra (dark gray), In^{3+} ions, and Sb^{5+} ions were displayed in a hexagonal unit cell. Oxygen ions around In^{3+} and Sb^{5+} ions are omitted. Exchange interactions, J_1 through J_4 , are labeled in different colors. The thickness of each path indicates the magnitude of the exchange interaction. (b) Buckled honeycomb network formed by the dominant exchange interaction J_1 projected along the c axis.

a magnetic field was applied perpendicular to the spin rotation plane by assuming additional DM interactions with the staggered vector component along the polar c -axis [28]. However, the neighboring exchange interactions J_1 and J_2 in Fig. 1 (a) were proposed to be equivalent by Raman spectroscopy [34], leading to uniform DM interaction instead of staggered one along the polar axis. To verify the scenario of the soliton lattice, identification of precise spin Hamiltonian by measuring the spin excitation in large momentum - energy space is required.

Here we performed inelastic neutron scattering (INS) experiments on polycrystalline sample of $\text{Ni}_2\text{InSbO}_6$ at zero magnetic field. Well-defined spectra were observed and successfully analyzed by linear spin-wave theory. The estimated exchange constants, J_1 and J_2 , were different by a factor of 6, supporting the scenario of the soliton lattice induced by the staggered DM interaction. In addition, chirality-induced DM interaction was discussed by combination of the present spin model and previously reported propagation vector. The estimated critical field applied parallel to the c axis was consistent with the previous study [28].

II. EXPERIMENTAL DETAILS

Polycrystalline sample of $\text{Ni}_2\text{InSbO}_6$ with a mass of 21 g was synthesized by solid-state reaction method. The polycrystalline sample wrapped by aluminum foil were sealed in an Al cell. A Gifford-McMahon type cryostat was used to control the temperature down to 10 K. An inelastic neutron scattering experiment was performed by using High Resolution Chopper (HRC) spectrometer [35] installed at BL-12 in MLF, J-PARC. The frequency of the T0 chopper was 50 Hz. The frequency of the Fermi chopper was 200 Hz, and the incident energies, E_i s, of 12.5, 15.3, 30.5, 61.2, and 102 meV were used for measurements at $T = 10$ K. An additional E_i of 61.2 meV was used for the measurements at $T = 10$ K, 35 K, 65 K, 100 K, 300 K. The data reduction was performed by HANA software [36].

III. EXPERIMENTAL RESULTS

Temperature dependence of inelastic neutron scattering spectrum with $E_i = 61.2$ meV is shown in Figs. 2(a)-2(d). E and Q denote the energy transfer and the momentum transfer, respectively. Well-defined spin-wave excitations with a band energy of 20 meV are observed at 10 K and 65 K which are below T_N . The intensity at 65 K is weaker because the sub-lattice moment is reduced near T_N . The spectrum at 100 K is smeared, nevertheless the remnant feature of spin-wave excitation is observed due to short-range spin correlation, which is characteristic of a low-dimensional spin system. The spectrum at 300 K, which is well above T_C , is featureless for $Q \lesssim 2 \text{ \AA}^{-1}$. The observed excitations for $Q \gtrsim 2 \text{ \AA}^{-1}$ are due to phonons.

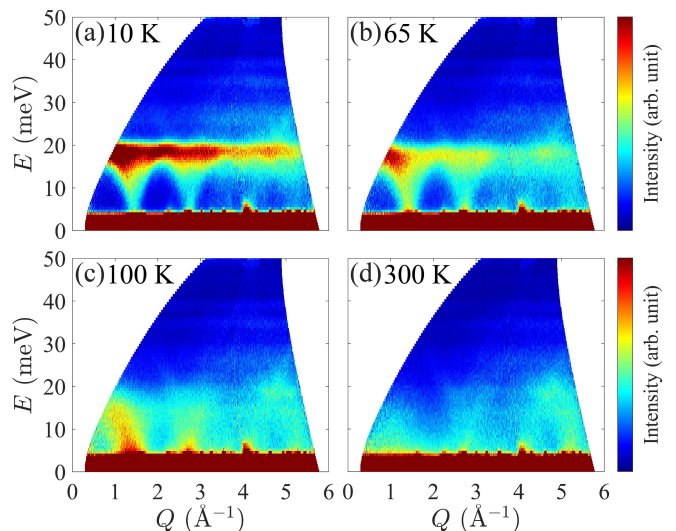


FIG. 2. Inelastic neutron scattering spectra with the incident energy $E_i = 61.2$ meV measured at (a) 10 K, (b) 65 K, (c) 100 K, and (d) 300 K.

The detailed structure of the spectrum with $E_i = 30.5$ meV at 10 K is shown in Fig. 3(a). Spin-wave excitation with no anisotropy gap is observed in the energy range of $E \gtrsim 2$ meV. The anisotropy gap is not observed in the range of $E \gtrsim 0.6$ meV in the spectrum with $E_i = 12.5$ meV as well (not shown).

IV. SIMULATION

Simulation of spin-wave excitation for $\text{Ni}_2\text{InSbO}_6$ was performed based on linear spin-wave theory (LSWT) using SpinW package [37]. Analytic approximation was adopted for the magnetic form factor of Ni^{2+} ions [38]. In this section we identify the main part of the spin Hamiltonian which dominates the observed spin spectra. In our simulation we used a Heisenberg spin model without DM interaction terms and a collinear antiferromagnetic spin structure was assumed as the ground state, since the incommensurability of the spin structure is as small as 0.04 \AA^{-1} , which is also hard to be probed by the present experiment. DM interaction crucial for the phase diagram will be discussed by a combination of the present INS experiment and the previous studies on neutron diffraction and bulk property measurements in the forthcoming section.

The Heisenberg spin Hamiltonian is represented as

$$\mathcal{H} = \sum_{\langle i,j \rangle} J(\mathbf{r}_i - \mathbf{r}_j) \mathbf{S}_i \cdot \mathbf{S}_j, \quad (1)$$

where \mathbf{r}_i is the position of i th Ni^{2+} ion and \mathbf{S}_i is the spin operator at the i th Ni^{2+} ion. The sum is taken over pairs of spins. In the crystal structure, two kinds of inequivalent Ni^{2+} ions denoted by Ni(1) and Ni(2)

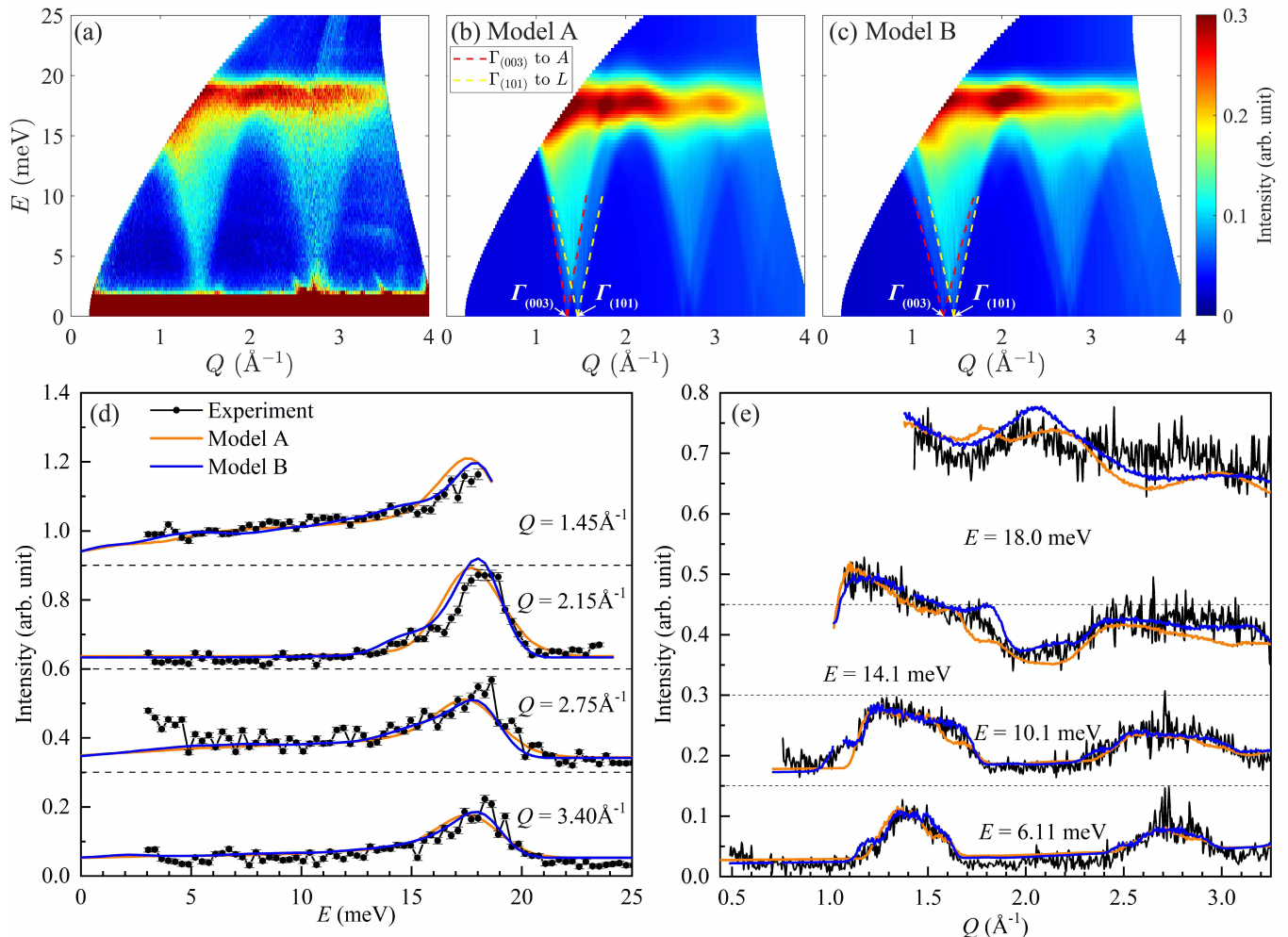


FIG. 3. (a) INS spectrum with $E_i=30.5$ meV at $T=10$ K. (b), (c) Calculated INS spectra of polycrystalline sample using the best fit parameters for model A in (b) and model B in (c). Modes of spin wave excitation from $\Gamma_{(003)}$ to A and from $\Gamma_{(101)}$ to L points are described by red and yellow dash lines, respectively. The incoherent elastic scattering below 3 meV is excluded from the fitting area. (d),(e) 1D cuts along the energy transfer in (d) and those along the momentum transfer in (e), where orange and blue lines indicate the simulations using model A and model B, respectively.

are stacked along the c -axis, three of each ion are contained in the hexagonal unit cell, as shown in Fig. 1(a). The first and second neighbor exchange interactions occur via the Ni-O-Ni path, whereas the third and fourth neighbor exchange interactions occur via the Ni-O-O-Ni path; all bond angles are obtuse, suggesting antiferromagnetic super-exchange interactions for all the cases. The first, second, third and fourth neighbor interactions are denoted by J_1 , J_2 , J_3 and J_4 , shown in Fig. 1(a). The labels for the spin model used here are the same as those in Ref. [34].

We tried a couple of models to fit the observed spectrum with $E_i = 30.5$ meV in Fig. 3(a). In model A the constraints $J_1 = J_2$ and $J_3 = J_4$ are imposed. The model is based on the crystal structural consideration that the atomic distances for the first (third) and second (fourth) neighbored Ni pairs and the relevant Ni-O-Ni (Ni-O-O-Ni) bond angles are similar, as shown in TA-

TABLE I. Atomic distances and bond angles for exchange paths in $\text{Ni}_2\text{InSbO}_6$. The exchange paths J_3 and J_4 go through two intervening oxygen atoms

| | J_1 | J_2 | J_3 | J_4 |
|---------------------------------------|--------|--------|-------|-------|
| Ni-Ni (\AA) | 3.747 | 3.876 | 5.216 | 5.216 |
| $\angle\text{Ni-O-Ni}(\text{^\circ})$ | 128.34 | 134.95 | - | - |

BLE. I. Previous Raman scattering study [34] used this model. In model B no constraint is imposed. The calculated spectra using the best fit parameters for the models are shown in Figs. 3(b) and 3(c). The experiment and calculation of the one-dimensional (1D) cuts along the energy axis and those along the momentum axis are shown in Fig. 3(d) and 3(e), respectively. The best parameters are summarized in Table II (see appendix A for the detail of the fitting). The model B gives a better correlation co-

TABLE II. Estimated exchange constants in the unit of meV, χ^2 , and correlation coefficient R for spin models.

| | J_1 | J_2 | J_3 | J_4 | χ^2 | R |
|---------|-------|-------|-------|-------|----------|-------|
| Model A | 3.56 | | 0.37 | | 8.8 | 0.928 |
| Model B | 6.05 | 0.95 | 0.21 | 0.19 | 6.1 | 0.953 |

efficient R and χ^2 , where $\chi^2 = \frac{1}{N} \sum_i \frac{(S_i^{\text{exp}} - S_i^{\text{sim}})^2}{\epsilon_i^2}$ and ϵ_i is the experimental error for S_i^{exp} .

V. DISCUSSION

The spin wave excitation at 10 K is found to stem from $Q \sim 1.4 \text{ \AA}^{-1}$ in the spectrum in Fig. 3(a). The momentum approximately corresponds to reciprocal points (003) and (101), which are called $\Gamma_{(003)}$ and $\Gamma_{(101)}$, respectively. The observed excitation is the superposition of the modes from these Γ points.

In the powder INS spectrum, with the increase of Q , the radius of a sphere in the three-dimensional reciprocal space, the INS signal appears when the sphere touches a surface of spin wave dispersion with nonzero intensity. The spectrum, then, loses the intensity when the sphere surface departs from the dispersion surface. Fig. 4(a) shows the simulated intensity profile of a single crystal for model A sliced at $(h0l)$ plane and at $E = 10.1 \text{ meV}$. The simulated dispersions around Γ points are ellipses with major axes laying along the a^* -axis. For Model B in Fig. 4(b), on the contrary, the major axes lay along the c^* -axis. These features are caused by the fast and slow velocities of spin waves along the c^* -axis for Model A and Model B, respectively. Considering the geometrical relation, the Q positions of contact and departure between the momentum sphere and dispersion ellipse around $\Gamma_{(101)}$ are almost indistinguishable for Model A and Model B: contact at $Q \sim 1.18 \text{ \AA}^{-1}$ and departure at $Q \sim 1.74 \text{ \AA}^{-1}$. In contrast around $\Gamma_{(003)}$, the positions are determined by the dispersion along the c^* -axis, leading to a significant difference: contacts at $Q \sim 1.13 \text{ \AA}^{-1}$ for model A and $Q \sim 1.01 \text{ \AA}^{-1}$ for model B, and departures at $Q \sim 1.56 \text{ \AA}^{-1}$ for model A and $Q \sim 1.69 \text{ \AA}^{-1}$ for model B. In the powder-averaged profile in Fig. 4(c), the calculation based on model B indicated by the blue curve has a shoulder structure at $Q \sim 1.01 \text{ \AA}^{-1}$, ascribed to the different contact Q s between the dispersions from $\Gamma_{(003)}$ and $\Gamma_{(101)}$. In contrast the calculation based on model A indicated by the orange curve does not have a shoulder structure at $Q \sim 1.01 \text{ \AA}^{-1}$ because the contact Q s for the dispersions from $\Gamma_{(003)}$ and $\Gamma_{(101)}$ are similar to each other. At $Q \sim 1.7 \text{ \AA}^{-1}$ the shoulder is absent for model B and present for model A. This is understood by considering the departure of the Q sphere from the spin dispersion for each model. The experimental profile indicated by the black curve is reproduced better by model B than by model A. By combination with better coeffi-

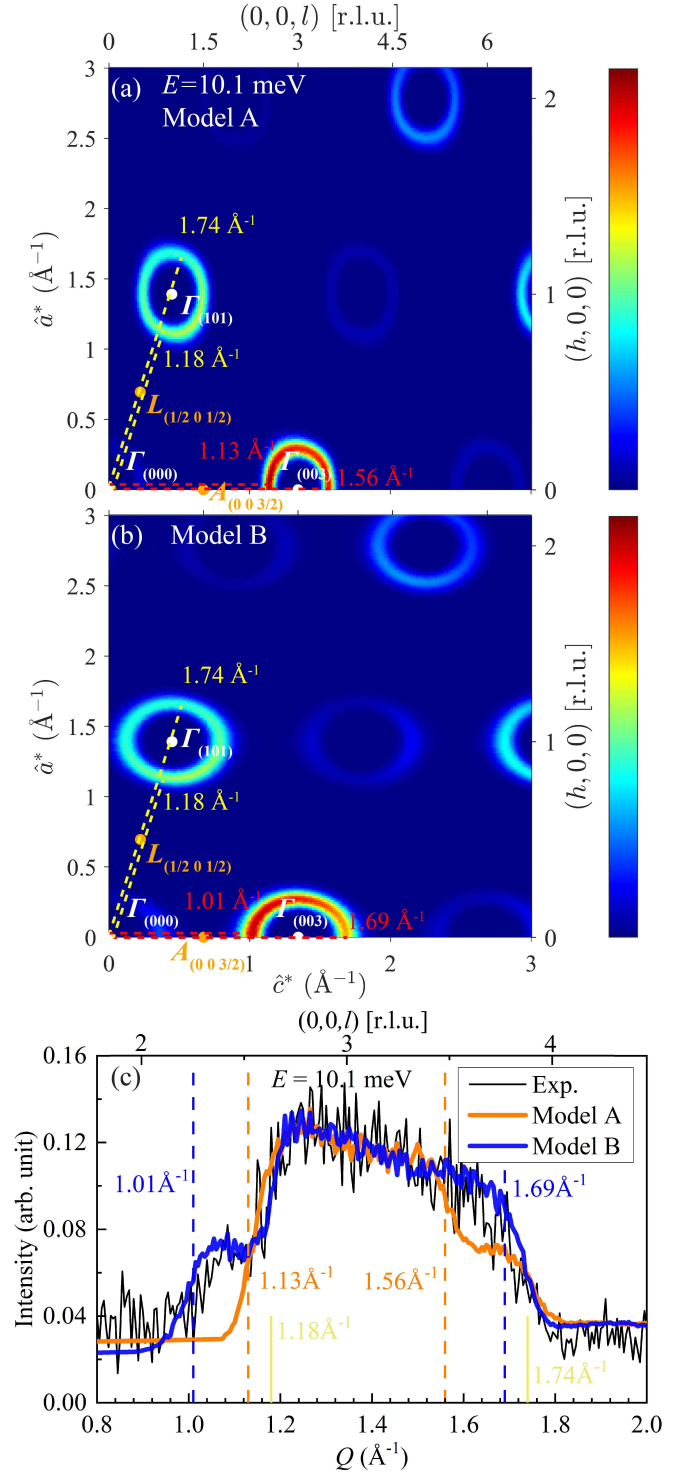


FIG. 4. (a),(b) Simulated spectra of single crystal slice at $E = 10.1 \text{ meV}$ for Model A (a) and Model B (b). High symmetry points, Γ , A , and L are marked. The dash lines denote the radius of momentum sphere first touches and departs the dispersion of ellipses. (c) 1D-cut of powder spectrum at $E = 10.1 \text{ meV}$ for experiment (black), model A (orange) and model B (blue). The vertical dashed orange (blue) lines indicate positions of the first touches and departures around $\Gamma_{(003)}$ for model A (B). The solid yellow lines indicate those around $\Gamma_{(101)}$ for both models A and B.

icients of χ^2 and R for model B, we can safely conclude that model B is more appropriate than model A.

The spin model in $\text{Ni}_2\text{InSbO}_6$ turns out to be a coupled two-dimensional (2D) honeycomb lattice stacked along the c -axis with intraplane interaction J_1 of 6.05 meV and interplane interaction J_2 of 0.95 meV. The difference between J_1 and J_2 is inconsistent with Raman scattering study [34] but consistent with the first principle calculation (GGA+U) for the isostructural compound Ni_3TeO_6 [39]. It should be noted here that J_4 and J_5 in Ni_3TeO_6 in Ref. 39 correspond to J_1 and J_2 in $\text{Ni}_2\text{InSbO}_6$ in the present study, respectively.

The third and fourth neighbor interactions in honeycomb lattice, J_3 for Ni(1) and J_4 for Ni(2), are both antiferromagnetic, leading to competition with antiferromagnetic J_1 and J_2 . The magnitudes of J_3 and J_4 , however, are not large enough to induce IC structure. Indeed in an isolated classical honeycomb lattice, $J_2/J_1 \gtrsim 0.2$ is required for the IC structure [40, 41]. DM interaction instead of geometrical frustration is the major origin of the helical magnetism in $\text{Ni}_2\text{InSbO}_6$.

DM interactions having polar and chiral components are allowed between Ni ions connected by J_1 and J_2 bonds from the crystallographic symmetry. Now that J_1 and J_2 are different by a factor of 6, the magnitudes of the corresponding DM interactions are different as well. The staggered magnitude of the chiral component of the DM interaction induces staggered magnetization along the propagation direction of the helix at zero magnetic field. In the circumstance, the spin soliton lattice can be induced in the field applied along the helix axis. This agrees with the proposed scenario of the spin soliton lattice in Ref. 28.

Based on the mean field (MF) theory, Weiss temperature is estimated to be -171.6 K by using the exchange parameters of model B. In previous magnetic susceptibility measurements, Weiss temperatures were estimated as -207 K and -188 K for magnetic field $H \perp c$ and $H \parallel c$, respectively [28]. The small discrepancy can be explained by the low dimensionality of the spin system or the weak frustration. With a decrease in temperature, the susceptibility of a quasi-2D spin model increases more moderately than that in 3D model owing to short-range antiferromagnetic spin correlation, which leads to a larger estimate of Weiss temperature.

Though the present INS experiments with relax Q resolution do not probe the helimagnetic order, we can estimate the chiral component of DM vector along the propagation of the helix from the reported propagation vector. The calculation of MF energy gives the spin-flop field in the field applied along the c axis $H_c = 18.3$ T (see Appendix B in detail). The estimate is consistent with the critical field, 16 - 19 T, previously reported in the magnetization measurements [28].

VI. CONCLUSION

Inelastic neutron scattering experiment was performed on a proper-screw-type helimagnet $\text{Ni}_2\text{InSbO}_6$ at zero magnetic field using a polycrystalline sample. Well-defined spin-wave excitation was observed. The obtained spectrum was carefully compared with the simulated spectra by linear spin-wave theory on the basis of two spin models: a three-dimensional spin model with the constraint $J_1 = J_2$ and a coupled honeycomb spin lattice model with $J_1 \neq J_2$. The latter model with $J_1 = 6.05$ meV and $J_2 = 0.95$ meV well reproduced the observed spectrum. The difference between J_1 and J_2 leads to staggered DM interactions along the polar c axis, which is the basis of the soliton lattice scenario in the field applied perpendicular to the c axis. The critical field of the spin-flop transition in the field applied parallel to the c axis estimated by MF calculation was consistent with the previous magnetization measurement.

ACKNOWLEDGMENTS

We are grateful to D. Kawana, T. Asami, and R. Sugiyura for supporting us in the neutron scattering experiment at HRC and HER. The neutron experiment using HRC spectrometer at the Materials and Life Science Experimental Facility of the J-PARC was performed under a user program (Proposal No. 2021S01). The neutron experiment using HER at JRR-3 was carried out by the joint research in the Institute for Solid State Physics, the University of Tokyo (Proposal No. 21403). Z. Liu was supported by the Japan Society for the Promotion of Science through the Leading Graduate Schools (MERIT). This project was supported by JSPS KAKENHI Grant Numbers 19KK0069, 20K20896 and 21H04441.

Appendix A: Fitting Details

The calculated spin-wave spectrum was modified by introducing a spin-wave lifetime and background. The fitting function is:

$$S^{\text{sim}}(Q, E) = A_1 \hat{S}^{\text{sim}}(Q, E) + A_2 \cdot Q^2 + A_3. \quad (\text{A1})$$

Here $\hat{S}^{\text{sim}}(Q, E)$ is the simulated structure factor convoluted by Gaussian function with FWHM = 2Γ , A_1 is the normalization factor, and the second and third terms stand for background. Γ includes both the instrumental energy resolution and the energy linewidth generated by spin wave lifetime. The best fitting results were obtained by minimizing χ^2 .

The fitting region was selected as $0.8 \text{ \AA}^{-1} < Q < 3.55 \text{ \AA}^{-1}$ and $3.05 \text{ meV} < E < 25.0 \text{ meV}$ of the experimental data to exempt incoherent elastic scattering. The best fitting result for model A is $J_1 = J_2 = 3.56$ meV, $J_3 = J_4 = 0.37$ meV, $\Gamma = 2.030$ meV and $\chi_A^2 = 8.8165$

(correlation coefficient $R_A = 0.9283$). The best result for model B is $J_1 = 6.05$ meV, $J_2 = 0.95$ meV, $J_3 = 0.21$ meV, $J_4 = 0.19$ meV, $\Gamma = 1.622$ meV and $\chi_B^2 = 6.0843$ (correlation coefficient $R_B = 0.9533$). The evaluation coefficients $\chi_A^2 > \chi_B^2$ and $R_A < R_B$ showed a better fitting for model B than for model A.

Appendix B: Spin-Flop Field

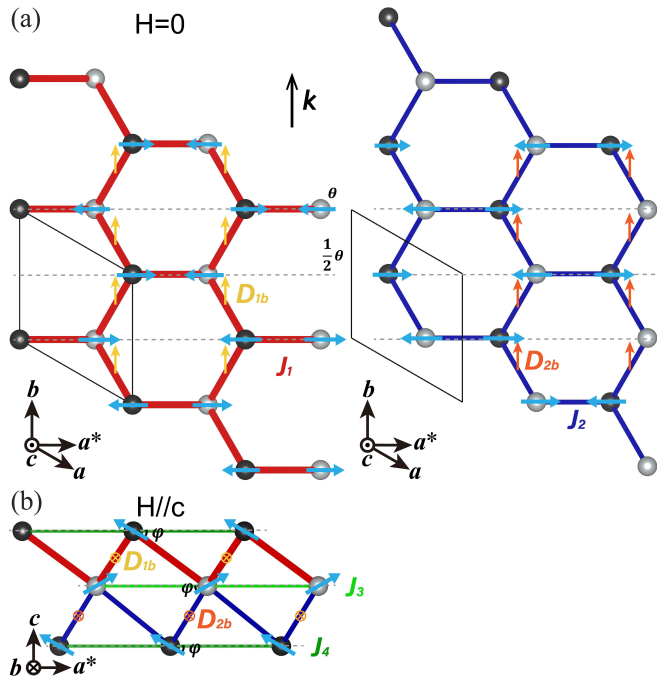


FIG. 5. (a) Proper-screw-type spin structure at zero field in a $\mathbf{k} \parallel \mathbf{b}$ microscopic domain. The light blue arrows represent the component of Ni^{2+} spin moments in the ab -plane, and they were scaled up for visualization. The spin rotates by θ with propagating distance b . D_{1b} and D_{2b} are the chiral components of DM vectors. (b) Canted Antiferromagnetic structure in $\mathbf{H} \parallel \mathbf{c}$.

The reported propagation vector \mathbf{k} is isotropic in the c -plane in the small-angle soft-X-ray scattering and neu-

tron diffraction experiment [28]. This means that the compound is in a multi-domain state, which is sensitive to a weak external field such as strain and a magnetic field. Here we consider a domain with $\mathbf{k} \parallel \mathbf{b}$ where the spin moments rotate in the a^*c -plane. We calculated the mean-field energy E_{helix} at zero field for the spin model shown in Fig. 5(a),

$$E_{\text{helix}}(\theta) = -(J_1 + J_2)S^2(1 + 2 \cos \frac{1}{2}\theta) + (J_3 + J_4)S^2(\cos \theta + 2 \cos \frac{1}{2}\theta) - 2(D_{1b} + D_{2b})S^2 \sin \frac{1}{2}\theta. \quad (\text{B1})$$

Here θ is defined as the rotation angle with propagating distance b . D_{1b} and D_{2b} are chiral components of DM vectors that induce helical structure along the b -axis. The c^* -axis components of the DM vectors which may induce staggered weak canted magnetization along the b -axis at zero field were neglected because the canted magnetization has been difficult to be observed. We solved the equation $(\frac{\partial E_{\text{helix}}}{\partial \theta})_{\theta=\theta_0} = 0$ where θ_0 was the rotation angle between the neighboring spins under the assumption that the D/J values are common for the bonds J_1 and J_2 . We, then, obtained $D_{1b} = 0.530$ meV and $D_{2b} = 0.083$ meV.

To estimate the spin-flop field in the field applied parallel to the c axis, we made an assumption that the helical spin structure was not changed by the magnetic field below the spin-flop field and the MF energy held. In addition, we assumed a canted antiferromagnetic structure (shown in Fig. 5(b)) which is a standard structure reported in helimagnets when the field is applied in the spin rotation plane [42, 43]. Then, the MF energy E_{CAF} is

$$E_{\text{CAF}}(\varphi) = -3(J_1 + J_2)S^2 \cos 2\varphi + 3(J_3 + J_4)S^2 - (D_{1b} - D_{2b})S^2 \sin 2\varphi - g\mu_B H S \sin \varphi, \quad (\text{B2})$$

where φ is the canted angle. We solved the equations $\frac{\partial E_{\text{CAF}}}{\partial \varphi} = 0$ and $E_{\text{helix}} = E_{\text{CAF}}$, and $\varphi = 0.039$ rad and critical field $H_c = 18.3$ T were obtained. Here $g = 2.26$ was used for Ni ions according to magnetization experiments in Ref. [22].

[1] T. Moriya, Anisotropic superexchange interaction and weak ferromagnetism, Phys. Rev. **120**, 91 (1960).
[2] I. Dzyaloshinsky, A thermodynamic theory of "weak" ferromagnetism of antiferromagnetics, J. Phys. Chem. Solids **4**, 241 (1958).
[3] I. Dzyaloshinskii, Theory of helicoidal structures in antiferromagnets. i. nonmetals, Sov. Phys. JETP **19**, 960 (1964).
[4] W. C. Koehler, J. W. Cable, M. K. Wilkinson, and E. O. Wollan, Magnetic structures of holmium. i. the virgin state, Phys. Rev. **151**, 414 (1966).

[5] K. Adachi, N. Achiwa, and M. Mekata, Helical magnetic structure in CsCuCl_3 , J. Phys. Soc. Japan **49**, 545 (1980).
[6] I. Sosnowska, T. P. Neumaier, and E. Steichele, Spiral magnetic ordering in bismuth ferrite, J. Solid State Phys. **15**, 4835 (1982).
[7] D. F. McMorrow, D. A. Jehan, R. A. Cowley, P. P. Swaddling, R. C. C. Ward, M. R. Wells, N. Hagmann, and K. N. Clausen, Helical magnetic order and spin slips in holmium-yttrium superlattices, Europhys Lett. **23**, 523 (1993).

- [8] K. Hamacher, H. Kaiser, J. Rhyne, K. Ritley, C. Flynn, and K. Theis-Bröhl, Neutron diffraction study of magnetic properties of Dy/Y superlattices, *Physica B Condens. Matter* **241-243**, 719 (1997), proceedings of the International Conference on Neutron Scattering.
- [9] G. Lautenschläger, H. Weitzel, T. Vogt, R. Hock, A. Böhm, M. Bonnet, and H. Fuess, Magnetic phase transitions of MnWO_4 studied by the use of neutron diffraction, *Phys. Rev. B* **48**, 6087 (1993).
- [10] A. Zheludev, S. Maslov, G. Shirane, I. Tsukada, T. Masuda, K. Uchinokura, I. Zaliznyak, R. Erwin, and L. P. Regnault, Magnetic anisotropy and low-energy spin waves in the dzyaloshinskii-moriya spiral magnet $\text{Ba}_2\text{CuGe}_2\text{O}_7$, *Phys. Rev. B* **59**, 11432 (1999).
- [11] M. D. Lumsden, B. C. Sales, D. Mandrus, S. E. Nagler, and J. R. Thompson, Weak ferromagnetism and field-induced spin reorientation in $\text{K}_2\text{V}_3\text{O}_8$, *Phys. Rev. Lett.* **86**, 159 (2001).
- [12] Y. Togawa, T. Koyama, K. Takayanagi, S. Mori, Y. Kousaka, J. Akimitsu, S. Nishihara, K. Inoue, A. S. Ovchinnikov, and J. Kishine, Chiral magnetic soliton lattice on a chiral helimagnet, *Phys. Rev. Lett.* **108**, 107202 (2012).
- [13] S. M. Mohseni, S. R. Sani, J. Persson, T. N. A. Nguyen, S. Chung, Y. Pogoryelov, P. K. Muduli, E. Iacocca, A. Eklund, R. K. Dumas, S. Bonetti, A. Deac, M. A. Hofer, and J. Åkerman, Spin torque-generated magnetic droplet solitons, *Science* **339**, 1295 (2013).
- [14] S. Bordács, A. Butykai, B. G. Szigeti, J. S. White, R. Cubitt, A. O. Leonov, S. Widmann, D. Ehlers, H.-A. K. von Nidda, V. Tsurkan, *et al.*, Equilibrium skyrmion lattice ground state in a polar easy-plane magnet, *Sci. Rep.* **7**, 7584 (2017).
- [15] Y. Fujima, N. Abe, Y. Tokunaga, and T. Arima, Thermodynamically stable skyrmion lattice at low temperatures in a bulk crystal of lacunar spinel GaV_4Se_8 , *Phys. Rev. B* **95**, 180410 (2017).
- [16] I. Kézsmárki, S. Bordács, P. Milde, E. Neuber, L. Eng, J. White, H. M. Rønnow, C. Dewhurst, M. Mochizuki, K. Yanai, *et al.*, Néel-type skyrmion lattice with confined orientation in the polar magnetic semiconductor GaV_4Se_8 , *Nat. Mater.* **14**, 1116 (2015).
- [17] T. Kurumaji, T. Nakajima, V. Ukleev, A. Feoktystov, T.-h. Arima, K. Kakurai, and Y. Tokura, Néel-type skyrmion lattice in the tetragonal polar magnet VOSe_2O_5 , *Phys. Rev. Lett.* **119**, 237201 (2017).
- [18] X. Yu, Y. Onose, N. Kanazawa, J. H. Park, J. Han, Y. Matsui, N. Nagaosa, and Y. Tokura, Real-space observation of a two-dimensional skyrmion crystal, *Nature* **465**, 901 (2010).
- [19] S. Mühlbauer, B. Binz, F. Jonietz, C. Pfleiderer, A. Rosch, A. Neubauer, R. Georgii, and P. Böni, Skyrmion lattice in a chiral magnet, *Science* **323**, 915 (2009).
- [20] S. Seki, X. Z. Yu, S. Ishiwata, and Y. Tokura, Observation of skyrmions in a multiferroic material, *Science* **336**, 198 (2012).
- [21] X. Zhang, G. Zhao, H. Fangohr, J. P. Liu, W. Xia, J. Xia, and F. Morvan, Skyrmion-skyrmion and skyrmion-edge repulsions in skyrmion-based racetrack memory, *Sci. Rep.* **5**, 7643 (2015).
- [22] S. A. Ivanov, R. Mathieu, P. Nordblad, R. Tellgren, C. Ritter, E. Politova, G. Kaleva, A. Mosunov, S. Stefanovich, and M. Weil, Spin and dipole ordering in $\text{Ni}_2\text{InSbO}_6$ and $\text{Ni}_2\text{ScSbO}_6$ with corundum-related structure, *Chem. Mater.* **25**, 935 (2013).
- [23] Y. S. Oh, S. Artyukhin, J. J. Yang, V. Zapf, J. W. Kim, D. Vanderbilt, and S.-W. Cheong, Non-hysteretic colossal magnetoelectricity in a collinear antiferromagnet, *Nat. Commun.* **5**, 3201 (2014).
- [24] G.-H. Cai, M. Greenblatt, and M.-R. Li, Polar magnets in double corundum oxides, *Chem. Mater.* **29**, 5447 (2017).
- [25] I. Živković, K. Prša, O. Zaharko, and H. Berger, Ni_3TeO_6 —a collinear antiferromagnet with ferromagnetic honeycomb planes, *J. Condens. Matter Phys.* **22**, 056002 (2010).
- [26] J. W. Kim, S. Artyukhin, E. D. Mun, M. Jaime, N. Harrison, A. Hansen, J. J. Yang, Y. S. Oh, D. Vanderbilt, V. S. Zapf, and S.-W. Cheong, Successive magnetic-field-induced transitions and colossal magnetoelectric effect in Ni_3TeO_6 , *Phys. Rev. Lett.* **115**, 137201 (2015).
- [27] M. O. Yokosuk, A. al Wahish, S. Artyukhin, K. R. O’Neal, D. Mazumdar, P. Chen, J. Yang, Y. S. Oh, S. A. McGill, K. Haule, S.-W. Cheong, D. Vanderbilt, and J. L. Musfeldt, Magnetoelectric coupling through the spin flop transition in Ni_3TeO_6 , *Phys. Rev. Lett.* **117**, 147402 (2016).
- [28] Y. Araki, T. Sato, Y. Fujima, N. Abe, M. Tokunaga, S. Kimura, D. Morikawa, V. Ukleev, Y. Yamasaki, C. Tabata, H. Nakao, Y. Murakami, H. Sagayama, K. Ohishi, Y. Tokunaga, and T. Arima, Metamagnetic transitions and magnetoelectric responses in the chiral polar helimagnet $\text{Ni}_2\text{InSbO}_6$, *Phys. Rev. B* **102**, 054409 (2020).
- [29] L. J. Bannenberg, K. Kakurai, P. Falus, E. Lelièvre-Berna, R. Dalgliesh, C. D. Dewhurst, F. Qian, Y. Onose, Y. Endoh, Y. Tokura, and C. Pappas, Universality of the helimagnetic transition in cubic chiral magnets: Small angle neutron scattering and neutron spin echo spectroscopy studies of FeCoSi , *Phys. Rev. B* **95**, 144433 (2017).
- [30] J. S. White, Á. Butykai, R. Cubitt, D. Honecker, C. D. Dewhurst, L. F. Kiss, V. Tsurkan, and S. Bordács, Direct evidence for cycloidal modulations in the thermal-fluctuation-stabilized spin spiral and skyrmion states of GaV_4S_8 , *Phys. Rev. B* **97**, 020401 (2018).
- [31] A. Zheludev, S. Maslov, G. Shirane, Y. Sasago, N. Koide, and K. Uchinokura, Field-induced commensurate-incommensurate phase transition in a dzyaloshinskii-moriya spiral antiferromagnet, *Phys. Rev. Lett.* **78**, 4857 (1997).
- [32] B. Roessli, J. Schefer, G. A. Petrakovskii, B. Ouladdiaf, M. Boehm, U. Staub, A. Vorotinov, and L. Bezmaternikh, Formation of a magnetic soliton lattice in copper metaborate, *Phys. Rev. Lett.* **86**, 1885 (2001).
- [33] Y. Togawa, Y. Kousaka, K. Inoue, and J. Kishine, Symmetry, structure, and dynamics of monoaxial chiral magnets, *J. Phys. Soc. Japan* **85**, 112001 (2016).
- [34] M. A. Prosnikov, A. N. Smirnov, V. Y. Davydov, Y. Araki, T. Arima, and R. V. Pisarev, Lattice and magnetic dynamics in the polar, chiral, and incommensurate antiferromagnet $\text{Ni}_2\text{InSbO}_6$, *Phys. Rev. B* **100**, 144417 (2019).
- [35] S. Itoh, T. Yokoo, S. Satoh, S. Yano, D. Kawana, J. Suzuki, and T. J. Sato, High resolution chopper spectrometer (HRC) at J-PARC,

- Nucl. Instrum. Meth. A **631**, 90 (2011).
- [36] D. Kawana, M. Soda, M. Yoshida, Y. Ikeda, T. Asai, R. Sugiura, H. Yoshizawa, T. Masuda, T. Hawaii, S. Ibuka, T. Yokoo, and S. Itoh, YUI and HANA: Control and visualization programs for HRC in J-PARC, J. Phys. Conf. Ser. **1021**, 012014 (2018).
- [37] S. Toth and B. Lake, Linear spin wave theory for single-q incommensurate magnetic structures, J. Condens. Matter Phys. **27**, 166002 (2015).
- [38] A. J. Dianoux and G. H. Lander, *Neutron Data Booklet* (Institut Laue Langevin, 2003).
- [39] F. Wu, E. Kan, C. Tian, and M.-H. Whangbo, Theoretical analysis of the spin exchange and magnetic dipole-dipole interactions leading to the magnetic structure of Ni_3TeO_6 , Inorg. Chem. **49**, 7545 (2010).
- [40] S. Asai, M. Soda, K. Kasatani, T. Ono, M. Avdeev, and T. Masuda, Magnetic ordering of the buckled honeycomb lattice antiferromagnet $\text{Ba}_2\text{NiTeO}_6$, Phys. Rev. B **93** (2016).
- [41] S. Asai, M. Soda, K. Kasatani, T. Ono, V. O. Garlea, B. Winn, and T. Masuda, Spin dynamics in the stripe-ordered buckled honeycomb lattice antiferromagnet $\text{Ba}_2\text{NiTeO}_6$, Phys. Rev. B **96** (2017).
- [42] M. Tokunaga, M. Akaki, T. Ito, S. Miyahara, A. Miyake, H. Kuwahara, and N. Furukawa, Magnetic control of transverse electric polarization in BiFeO_3 , Nat. Commun. **6**, 5878 (2015).
- [43] B. Ruetz, S. Zvyagin, A. P. Pyatakov, A. Bush, J. F. Li, V. I. Belotelov, A. K. Zvezdin, and D. Viehland, Magnetic-field-induced phase transition in BiFeO_3 observed by high-field electron spin resonance: Cycloidal to homogeneous spin order, Phys. Rev. B **69**, 064114 (2004).